



Development of novel mesoporous C–TiO₂–SnO₂ nanocomposites and their application to anode materials in lithium ion secondary batteries

Yuanyuan Zhou^{a,1}, Changshin Jo^b, Jinwoo Lee^b, Chul Wee Lee^{a,1}, Guanjun Qao^c, Songhun Yoon^{a,*}

^a Green Chemical Technology Division, Korea Research Institute of Chemical Technology (KRICT) and University of Science and Technology (UST), Daejeon 305-600, Republic of Korea

^b Department of Chemical Engineering, Pohang University of Science and Technology, Kyungbuk 790-784, Republic of Korea

^c State Key Laboratory for Mechanical Behavior of Materials, Xi'an Jiaotong University, Xi'an 710049, PR China

ARTICLE INFO

Article history:

Received 9 August 2011

Received in revised form 4 October 2011

Accepted 23 October 2011

Available online 3 November 2011

Keywords:

Ordered mesoporous materials

TiO₂

SnO₂

Anode

Lithium ion batteries

ABSTRACT

Herein, we employed the tetra-constituent co-assembly method based on the acid–base pair of Sn and Ti precursors. Using this method, novel mesoporous carbon–TiO₂–SnO₂ nanocomposite materials were prepared and their structural change with an increase of SnO₂ amount was investigated. In low amount of SnO₂, an ordered mesoporous structure was observed but it became collapsed at 64 wt.% SnO₂, while crystal size of anatase TiO₂ embedded within amorphous SnO₂ and carbon matrix became larger. When applied to anode materials in lithium ion batteries, an increase of the reaction peaks of Li⁺ in SnO₂ was observed and peak associated with discharging in TiO₂ nano-crystal increased in spite of lower amount of TiO₂. This indicated that TiO₂ was highly utilized for lithium storage (275 mAh g⁻¹ in 19.9 wt.% TiO₂ case). In the nanocomposite electrode with 28.8% TiO₂, however, a high rate performance and a very stable cycle performance (95.3% retention at 40th cycles) were observed, which was attributed to the stable nanostructure.

© 2011 Elsevier Inc. All rights reserved.

1. Introduction

Recently, the investigation about ordered mesoporous carbon (OMC) composite materials containing electrochemically active metal oxides has been vastly tried in order to apply into the anodes in lithium ion batteries (LIBs) [1–5]. It has been clarified that they have the beneficial features as anode materials. First, the high rate capability was attainable due to the fast diffusion of lithium ions within the nanosized pore walls and the easy transport of electrolyte through the ordered mesopores. Also, the charge accumulation at charge storage sites was facile due to the high surface area [1–6]. Among various metal oxides which can store lithium ions as anodes, several candidates such as CoO, SnO₂ and TiO₂ have been investigated as the nanocomposites with OMC [1–5]. Although it has been reported that OMC–TiO₂ nanocomposite electrodes have exhibited an improved anode performance, their intrinsically low capacity (~200 mAh g⁻¹) can be one of the shortcomings of their anode application [2,6]. In order to overcome this, the nanocomposite with other metal oxides such as SnO₂, SbO₂ and SiO₂ was investigated, where a larger charge storage was observed due to its alloying reaction with lithium ion. Most research on OMC/TiO₂ or SnO₂ has employed a post-addition of Sn or Ti sources into

the pores of OMC materials, which can give rise to the formation of inhomogeneous and bulky metal oxide crystals after thermal treatment of those composites [1,5].

In the typical preparation of carbon–TiO₂–SnO₂ nanocomposite (C–TiO₂–SnO₂), it has been reported that the crystal growth of TiO₂ and SnO₂ was severe due to the high carbonization temperature [1,5]. As for the crystal structure of TiO₂, various crystalline phases exist as rutile [7,8], anatase [9,10], TiO₂-B [11,12], brookite [13] and ramsdellite [14], which were applied as anode materials in lithium ion batteries. When they were prepared as nanostructures, high capacity from 200 to 300 mAh g⁻¹ was observed. Due to their structural instability, however, the high capacity above 200 mAh g⁻¹ was hard to maintain after long cycles. Although SnO₂ has a high theoretical capacity of 780 mAh g⁻¹, furthermore, the cycle performance was not satisfactory even after the nanostructure formation by the post-addition of Sn precursor into the OMC matrix, which was attributed to the large volume change of SnO₂ during charging–discharging [5]. In order to overcome these obstacles, it is highly required to prepare a complete C–TiO₂–SnO₂ nanocomposite by one-step process using carbon, Ti and Sn precursors. With this in mind, the tetra-constituent co-assembly (Tetra-CCA) method using Ti-citrate precursor was reported in our previous paper [3]. In this method, a block copolymer surfactant, oligomeric resol and silicate source were reacted with Ti-citrate solution. After aging and calcination, the C–TiO₂–SiO₂ nanocomposite containing ordered mesopores was obtained.

* Corresponding author. Tel.: +82 42 860 7199; fax: +82 42 860 7389/7381.

E-mail address: yoonsun@kRICT.re.kr (S. Yoon).

¹ Tel.: +82 42 860 7199; fax: +82 42 860 7381.

In order to prepare a mesoporous nanocomposite of carbon–TiO₂ and SnO₂ via one-step synthesis, herein, the tetra-constituent co-assembly (Tetra-CCA) method based on the acid–base pair concept is employed. It is expected that carbon skeleton which is helpful in maintaining an ordered structure makes a high electrical percolation network. An acid–base pair between Ti alkoxide and Sn chloride is added in order to avoid a formation of inhomogeneous metal oxide phase and make a stable nanostructure. Using the evaporation-induced self-assembly (EISA), a homogeneous film-type gel is obtained and heat-treated to produce an ordered mesoporous C–TiO₂–SnO₂ nanocomposites.

2. Experimental section

2.1. Preparation of composites

The resol as carbon precursor was prepared according to the literature [17]. The final resol precursors were dissolved in ethanol (20 wt.% ethanolic solution) for direct use. For Tetra-CCA preparation of C–TiO₂–SnO₂ nanocomposite, typically, 1 g of P123 (EO₂₀-PO₇₀EO₂₀, Aldrich, *Mw* = 5800) was dissolved in 20 g of ethanol under stirring until a clear solution was acquired. Then 0.973 g (3.6 mmol) of SnCl₄ (Aldrich) and 1.528 g (6.7 mmol) of Ti(OEt)₄ (Aldrich) was added dropwise under vigorous stirring separately. Upon stirring for 10 min, 2 g of 20 wt.% resol ethanolic solution was dropped slowly when the solution turned orange immediately. Upon further stirring for 2 h, the clear solution was poured into several Petri dishes and kept in a humidity-controlled ambient environment for full evaporation of ethanol. Afterwards the result film was polymerized at 100 °C for 24 h in an oven with a brittle transparent film forming. The as-prepared film was ground into fine powders, calcined at 450 °C for 2 h and further at 600 °C for 2 h under an inert atmosphere (N₂). After cooling down to the room temperature, the product was taken out, which produced Ti, Sn and carbon nanocomposite named as TSC-1. Similarly, a TSC-2 and a TSC-3 composite are prepared by adjusting the Sn/Ti molar ratio to 5:5 and 6.7:3.6 separately with the total molar amount of Ti and Sn maintained as 0.01 mol.

2.2. Characterization and anode performance investigation

The pore size distribution (PSD) was analyzed using an N₂ adsorption measurement (Micromeritics ASAP 2010). The external morphology of the carbon was examined using a scanning electron microscope (SEM, JEOL JSM-840A), whereas the pore image was scanned by a transmission electron microscope (TEM, JEOL JEM-2010). The energy dispersive X-ray analysis was conducted using the EDX analyzer equipped with the TEM in point mode and area mode. The X-ray diffraction (XRD) patterns were obtained with a Rigaku D/Max-3C diffractometer equipped with a rotating anode and Cu K_α radiation ($\lambda = 0.15418$ nm). X-ray photoelectron spectroscopy (XPS) experiments were carried out in an ultrahigh vacuum using the Scienta ESCA-300 high-resolution X-ray photoelectron spectrometer (HR-XPS).

For the preparation of composite anodes, the prepared materials were mixed with a conducting agent (Super P) and PVDF (polyvinylidene fluoride) binder with a weight ratio of 8:1:1. The mixture was then dispersed in NMP and spread on Cu foil (apparent areas of 1 cm²), followed by pressing and drying at 120 °C for 12 h. The half-cell characteristics was analyzed with a coin-type (CR2016) two electrode cell in which lithium foil (Cyprus Co.) was used. The electrolyte was 1.0 M LiPF₆ in ethylene carbonate (EC)/dimethyl carbonate (DMC) (1:1 volume ratio) (Technosemi Chem.). To investigate the anode performance in a lithium ion battery, a galvanostatic charge–discharge test in a voltage range of

2.5–0 V vs. Li/Li⁺ was conducted. For the rate performance measurement, the current was varied from 30 mA g⁻¹ to 300 mA g⁻¹. The cycle performance for 40 cycles was recorded at 30 mA g⁻¹. All of the electrochemical measurements were conducted using a WBCS-3000 battery cycler (Xeno Co.) at ambient temperature in a glove box filled with argon. For cyclic voltammetry measurement, a voltage range of 2.5–0 V vs. Li/Li⁺ was applied with scan rate of 0.2 mV s⁻¹. For the electrochemical impedance spectroscopy (EIS) measurement, a frequency range of 10⁶ Hz to 5 mHz was used with an ac amplitude of 10 mV (Ivium potentiostat) at 2 V vs. Li/Li⁺.

3. Results and discussion

In Fig. 1, the schematic explanation of the overall preparation is summarized. In this approach, Tetra-CCA method was employed in order to obtain a mesoporous nanocomposite that was composed of TiO₂, SnO₂ and carbon. As carbon precursor, PF resol was added for the purpose of increasing the structural strength of mesoporous structure forming an amorphous glue-like background for the controlled in situ crystallization of metal oxides and making a high electrical percolation within mesostructure [1,3,15,16]. As Ti and Sn precursor, Ti(OEt)₄ and SnCl₄ were utilized because an acid–base pair can be formed between them, which can have an interaction with P123 surfactant and also prevent isolated phases formation of metal oxides after high temperature sintering [17]. After the evaporation induced self-assembly (EISA) procedure, the composite was carbonized at 600 °C. During this step, an ordered mesoporous nanocomposite composed of C–TiO₂–SnO₂ was prepared. To the best of our knowledge, this is the first preparation of ordered mesoporous nanocomposite materials composed of carbon, TiO₂ and SnO₂ using simple one-step synthesis. In general, multi-step procedures have been utilized for the preparation of similar nanocomposites. In addition, the prepared materials were applied as anode materials in lithium ion batteries. The weight fraction of TiO₂, SnO₂ and carbon was calculated by ICP methods, which was listed at Table 1.

Fig. 2 displays the small angle and wide angle X-ray diffraction (XRD) patterns. In TSC-1 material, a broad peak was observed at $2\theta = 0.7^\circ$, which was probably associated with a long-range ordering of mesopores. In TSC-2, the ordered peak became sharper and moved to a lower angle, indicative of increasing cell parameter. However, the ordered structure was collapsed and no peak was observed in TSC-3, which reflected that higher addition of SnCl₄ resulted in a collapse of ordered structure. Fig. 2(b) displays the wide angle XRD patterns. Interestingly, only anatase phase TiO₂ was observed and, no crystal structure of SnO₂ and carbon appeared. Note that the peak intensity for [101] plane of TiO₂ crystal became higher as SnO₂ increased, in spite of a decrease of TiO₂ weight fraction. This implies that SnO₂ and carbon remained amorphous, but the crystallinity of TiO₂ became higher according to an increase of SnO₂. This observed tendency in crystal structure is possibly relevant to the mole ratio between Ti and Sn. It has been reported that crystallinity of anatase TiO₂ was less developed than our TSC-1 in the case of mesoporous material having 80% carbon and 20% TiO₂, indicating that carbon phase retarded a crystal growth of TiO₂. In our experiment, on the contrary, a high interaction between carbon and SnO₂ could accelerate crystal growth of TiO₂ or the lower concentration of titania source could promote its crystal growth, which require a further investigation. In addition, there are small bumps at around $2\theta = 31^\circ$ for all the three samples, which corresponded to the rutile TiO₂ phase. Small amount of rutile phase formed during high-temperature calcination because of its high thermodynamic stability. Because nanosized rutile TiO₂ shows excellent capacity retention and a high

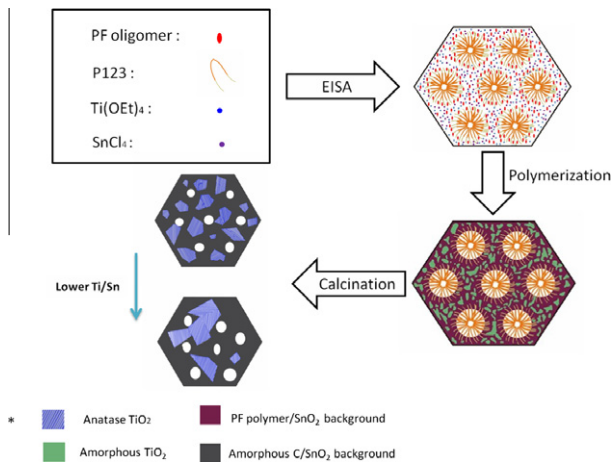


Fig. 1. Schematic explanation of mesoporous carbon-TiO₂-SnO₂ nanocomposite using tetra-constituent co-assembly method, which is based on the acid-base interaction between Ti and Sn precursors.

rate performance as lithium battery anode, it is expected that formation of small amount of rutile TiO₂ can possibly give additional benefit to our designed materials [3,7].

Fig. 3 shows the TEM images of the prepared materials. As can be seen, wormhole-like mesopores with a long range ordering appeared in TSC-1 and -2. Also, thick walls which consisted of TiO₂, SnO₂ and carbon are observed. This multi-components wall became thicker in accordance with an increase of SnO₂. From high resolution TEM images of **Fig. 3(b)**, (d) and (f), nanosized anatase TiO₂ crystals embedded within the amorphous SnO₂ and carbon matrix were observed. Their size became larger as SnO₂ increased, which coincided with wide-angle XRD results in **Fig. 2(b)**.

In order to confirm the uniform distribution of Ti and Sn metal within the mesoporous nanocomposites, elemental analysis using EDX for point and area modes were conducted for TSC-1 material, which was shown in **Fig. 4**. Carbon, Ti and Sn were located homogeneously within the ordered structures in TSC-1. In the literature, it was reported that small sized crystals of titania were observed after high temperature heat treatment (>400 °C) [15]. In our preparation, however, the crystal size of TiO₂ can be controlled by a change of SnCl₄ adding amount. Furthermore, the transition state of Ti and Sn was investigated by XPS analysis.

Fig. 5 displays XPS spectra for Ti 2p from 454 to 468 eV and Sn 3d spectra from 480 to 505 eV. As seen, the symmetric Ti 2p peaks at 458.9 and 464.6 eV indicate stoichiometric TiO₂ with a low concentration of defects. Ti 2p_{3/2} peak position at 458.9 eV in TSC-1 spectra is similar to that of pure TiO₂ (458.6 eV), reflecting that Ti in TSC-1 has +4 transition state (Ti⁴⁺) [18,19]. Similarly, peak positions of Sn 3d_{5/2} and 3d_{3/2} were located at 487.2 and 495.5 eV, respectively. This exhibited the oxidation state of amor-

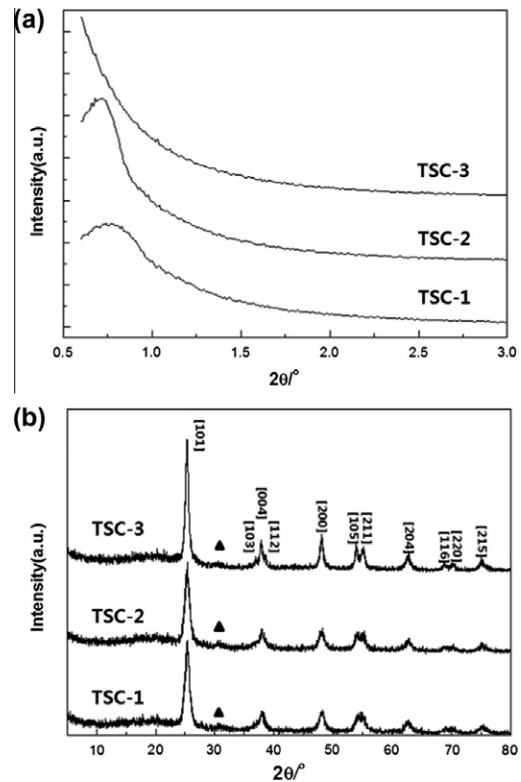


Fig. 2. (a) Small angle X-ray scattering patterns. (b) Wide angle X-ray diffraction patterns of the prepared materials. Insets are peak indexes of anatase TiO₂ and triangle is the index of rutile of TiO₂.

phous SnO₂ is nearly +4, which coincided with the peak positions of Sn 3d_{5/2} and 3d_{3/2} in nanoparticles (486.7 and 495.1 eV, respectively) [20].

In **Fig. 6(a)**, the N₂ sorption isotherms for TSC series are shown. Here, characteristic H₂ type hysteresis defined from IUPAC was commonly observed [23,24]. This hysteresis loop at around 0.5 P/P₀ was relevant to the mesopores, which became larger as SnO₂ increased. Note that a large increase of adsorbed volume in TSC-3 was observed. The pore size distributions (PSDs) by BJH method from the adsorption branch are given in **Fig. 6(b)**. For TSC-1 material, less-developed pore structure was observed, which was clearly improved in TSC-2 material. Three kinds of pores (2, 3.5 and 7 nm) were observed in TSC-3 materials, which was relevant to pore formation of interstitial sites between the large TiO₂ crystals and carbon/Sn amorphous phase. This abrupt formation of high mesoporosity can raise the collapse of ordered structure in TSC-3. This PSD change coincided with TEM image as shown in **Fig. 3**. From the crystallographic and morphological analysis conducted

Table 1
Results of structural and electrochemical analysis.

	TiO ₂ (wt.%)	SnO ₂ (wt.%)	C ^a (wt.%)	TiO ₂ /SnO ₂ ^b (molar ratio)	A _{BET} ^c (m ² g ⁻¹)	V _{meso} (cm ³ g ⁻¹)	V _{micro} (cm ³ g ⁻¹)	C _{ch} (mAh g ⁻¹)	C _{dis} (mAh g ⁻¹)	IE ^d (%)	Rate (%)	Cycle ^e (%)
TSC-1	42.3	37.7	20.0	2.11	232	0.042	0.078	629	229	36	49	79.9
TSC-2	28.8	53.9	17.2	1.01	235	0.054	0.076	901	277	31	53	95.3
TSC-3	19.9	63.9	16.2	0.59	281	0.079	0.091	883	378	43	45	81.0

^a The fraction of TiO₂, SnO₂ and C were obtained by TGA and ICP methods.

^b The molar ration of TiO₂/SnO₂ is converted from the mass ratio of TiO₂/SnO₂.

^c BET surface area (A_{BET}) and mesopore volume (V_{meso}), micropore one (V_{micro}) were obtained by N₂ sorption analysis.

^d Initial charging capacity (C_{ch}), discharging capacity (C_{dis}) and initial efficiency (IE) were obtained by galvanostatic charge-discharge experiment.

^e Rate capability was obtained by a comparison between the discharge capacities at 30 mA g⁻¹ and 300 mA g⁻¹. Cycle performance was estimated by discharge capacity after 40th cycles by that of first cycle.

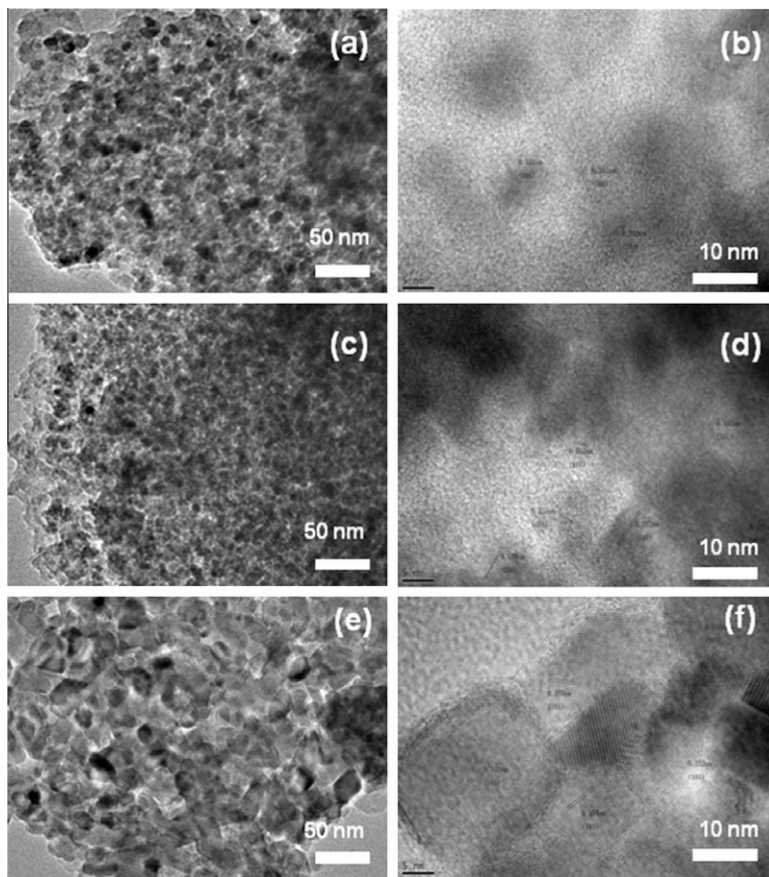


Fig. 3. TEM images of the prepared nanocomposite materials. TSC-1 (a) and (b); TSC-2 (c) and (d); TSC-3 (e) and (f).

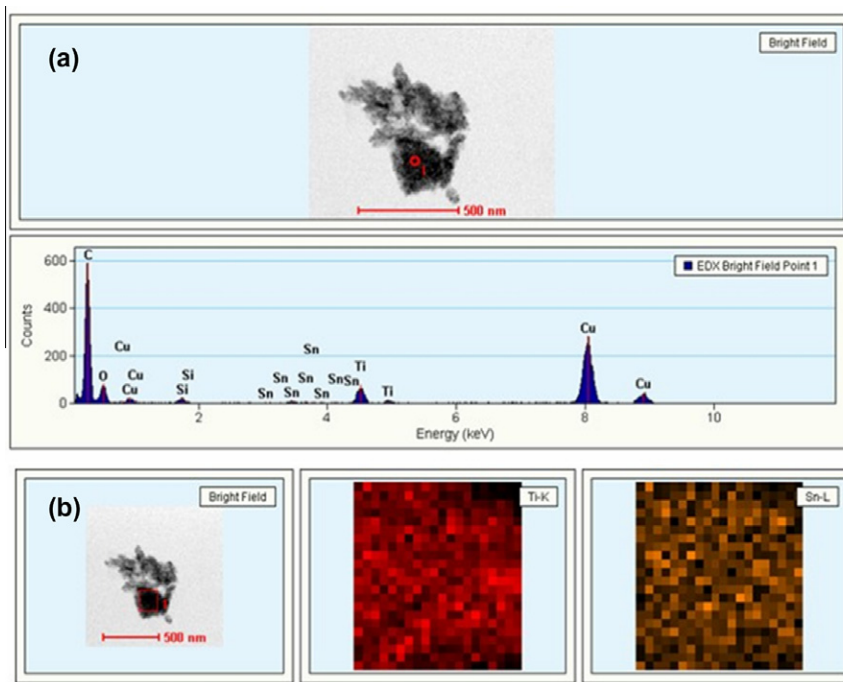


Fig. 4. EDX elemental analysis of TSC-1 for point mode (a) and area mode (b).

above, it was concluded that TiO_2 crystals became larger and the mesoporosity became more developed according to an increase of SnO_2 , while the ordered structure was collapsed.

Fig. 7 shows anode performance results of the TSC electrodes in the voltage range from 0 to 2.5 V vs. Li/Li^+ . The individual components of TiO_2 , SnO_2 and carbon in the prepared composite materi-

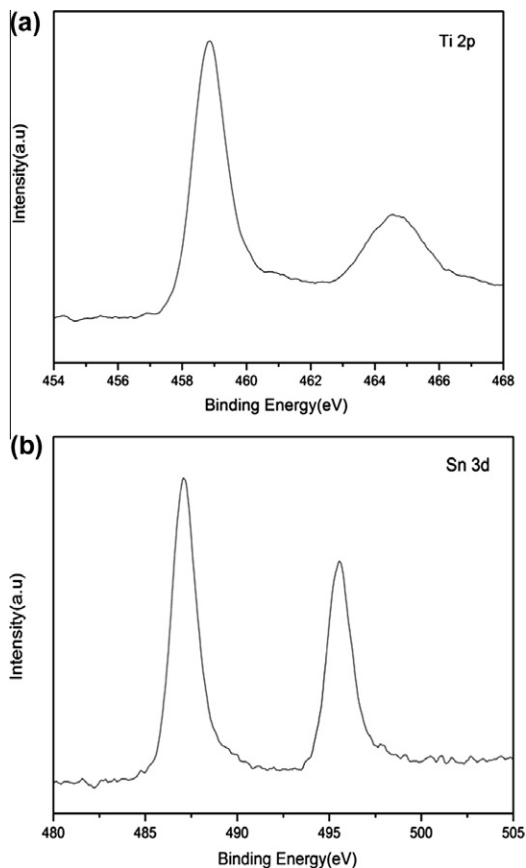


Fig. 5. XPS spectra for TSC-1 sample for Ti 2p (a) and Sn 3d (b).

als can make a different contribution in the capacity. Typically, the reversible capacities of SnO_2 and TiO_2 appear below and above 2 V, respectively, which are associated with their characteristic electrochemical reactions with Li^+ [7–12]. As for amorphous carbon, Li^+ can be stored uniformly at overall potential according to our previous research. As shown in Fig. 7(a), the galvanostatic charge–discharge profiles are shown. As can be seen, charging capacity (C_{ch}) became larger from 629 to 900 mAh g^{-1} and discharging capacity (C_{dis}) increased from 229 to 378 mAh g^{-1} as SnO_2 increased. This capacity increase is mostly due to a larger amount of SnO_2 , which has a 780 mAh g^{-1} theoretical capacity as the crystal phase [2,20]. As for the capacity of TiO_2 , it is known that be highly dependent on temperature of heat treatment, preparation method and morphology difference [7–14]. Capacity became smaller with an increasing temperature and the nanostructured TiO_2 electrodes exhibited an improved capacity while their cycle performance became poor [7–14]. Note that the reversible capacity of the amorphous carbon material which was prepared without addition of Sn and Ti precursor, was about 200 mAh g^{-1} (not shown here). In Fig. 7(a), interestingly, a plateau was observed in TSC-3 electrode in spite of its smaller weight fraction of TiO_2 (19.9 wt.%). In contrast, this plateau disappeared in TSC-1 electrode although it contained 42.3 wt.% TiO_2 . This unpredicted result is discussed later. In Fig. 7(b), cyclic voltammetry of TSC-2 electrode is displayed. From this figure, the characteristic two peaks at 0.5 and 2.3 V were observed in anodic scan in upward direction to higher voltage, which were attributed to the Li^+ discharge at SnO_2 and TiO_2 , respectively.

In Fig. 8, the differential capacity per voltage was plotted against potential, which was calculated from the discharge profiles in Fig. 7(a). This differential capacity per voltage is useful to separately analyze potential-dependent electrochemical reactions. As

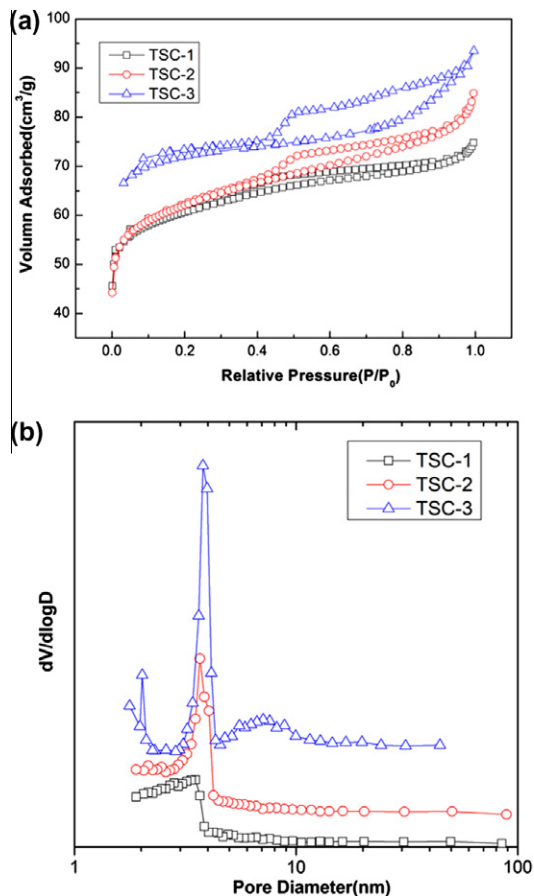
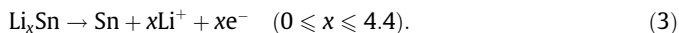
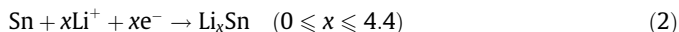


Fig. 6. (a) N_2 sorption isotherms for TSC-1, -2 and -3. (b) The pore size distribution from BJH adsorption branch of TSC-1, -2 and -3.

can be seen, two large peaks below 1.5 V and sharp peak near 2.2 V commonly appeared. As SnO_2 increased, two peaks below 1.5 V became larger and a higher peak near 2.2 V was observed while the position of the latter peak moved to a lower value. Moreover, a small peak at 1.7 V was observed in TSC-3 electrode. The changes of the electrochemical reaction peaks are associated with characteristic electrochemical reactions in SnO_2 and TiO_2 . Typically, electrochemical reaction for Li^+ storage in SnO_2 anode can be described as following equations [20]:



During the first charging (reduction) process to downward direction of potential, the reaction of Eq. (1) happens with reduction of SnO_2 to metallic Sn and Li_2O , which is known to be observed at 0.9 V during the first charging. As shown in Fig. 5(a), the capacity from Eq. (1) reaction became higher when SnO_2 increased. Then voltage declined continuously from 0.5 to 0.02 V, which can be attributed to the formation of different alloy phases, producing $\text{Li}_{4.4}\text{Sn}$ finally as shown in Eq. (2). During discharge process, typical two peaks at 0.5 and 1 V were observed in Fig. 6, which is relevant to de-alloying of lithium from $\text{Li}_{4.4}\text{Sn}$ (Eq. (3)). In the literatures, it has been reported that the peak at 0.5 V is main one while the latter peak is broad and weak [5,20]. On the contrary, the two peaks were similar in TSC-1 and -2 electrodes, but the peak at 1.0 V was very strong in TSC-3 sample, which was possibly due to nanocom-

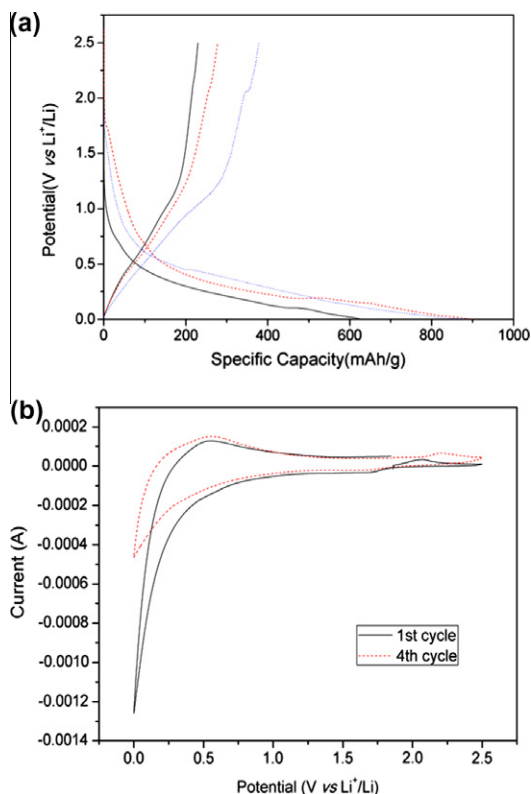


Fig. 7. (a) Galvanostatic charge–discharge profiles for TSC-1 (solid line), TSC-2 (dash line) and TSC-3 (dotted line) at 0.1 C rate. (b) Cyclic voltammetry of TSC-2 electrode at 0.2 mV s⁻¹ scan rate.

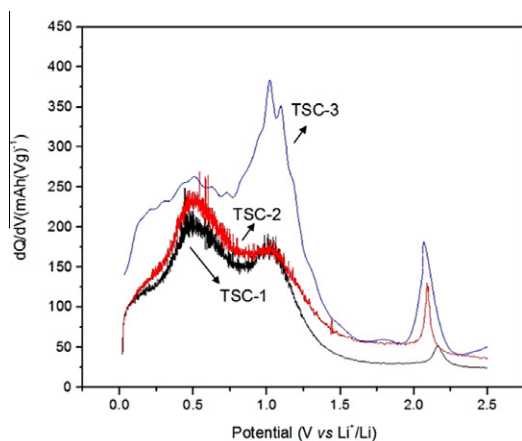


Fig. 8. Voltage dependency of differential capacity per voltage which was estimated by the discharge profile of Fig. 4(a) for TSC-1, TSC-2 and TSC-3.

posite effect with carbon and TiO₂. Similar to the materials which were prepared by SnO₂ incorporation into the pores of OMC, the reversible peak at 1.3 V was observed, which was associated with a reversible reaction of Eq. (1). When considering the theoretical capacity of SnO₂ (780 mAh g⁻¹), TSC-1 and -3 should show 294 and 498 mAh g⁻¹ discharge capacity above 1.7 V, respectively but a less capacity of 204 and 323 mAh g⁻¹ were observed, which was due to the amorphous nature of SnO₂ and an additional carbon content (~20 wt.%).

Another important feature in discharge peak in Fig. 8 is the increasing peak intensity near 2.2 V, which is related with the discharging process within TiO₂ phase [7–10]:

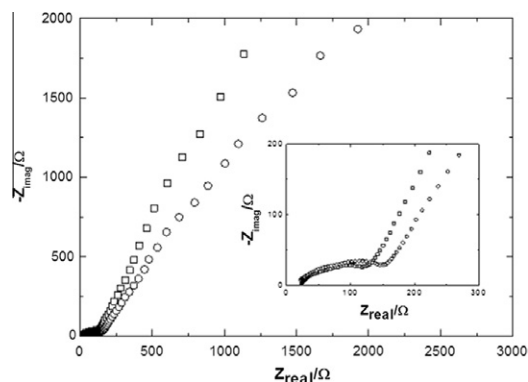


Fig. 9. EIS spectra TSC-1 (rectangle) and -3 (circle) electrodes at 2.0 V vs. Li/Li⁺ after 40 cycles.

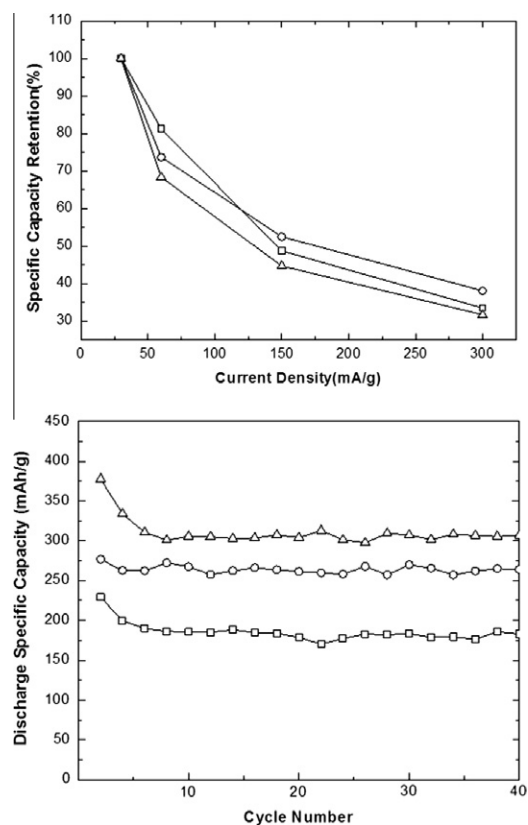


Fig. 10. Rate capability results (a) and cycle performance test (b) of TSC -1 (rectangle), -2 (circle) and -3 (triangle).



In the typical electrochemical reaction of anatase TiO₂ nanoparticle, x is known to be about 0.5 (160.8 mAh g⁻¹) [8,9]. As shown in Fig. 8, peak near 2 V became larger and moved to lower value according to SnO₂ increase. While the small peak in TSC-1 electrode indicated a low capacity, a large capacity was observed in TSC-3 electrode in spite of less weight fraction of TiO₂ (19.9%), indicative of its higher utilization for Li⁺ charging. From approximate calculation, C_{dis} above 1.7 V of TSC-1 and -3 were 25 and 55 mAh g⁻¹, which reflected that discharge capacities by TiO₂ itself were 67 and 275 mAh g⁻¹, respectively. This is probably attributed to more available Li⁺ storage sites in well-developed TiO₂ crystals in TSC-3.

In order to investigate a change of lithium storage features, electrochemical impedance spectroscopy (EIS) was carried out for the TSC-1 and -3 electrodes in the 5×10^{-3} to 10^5 Hz frequency region at 2 V vs. Li/Li⁺. Fig. 9 displays the EIS spectra as Nyquist plots. Here, the EIS spectra comprised of one or two semi-circles in the high frequency region followed by a straight line with decreasing frequency, which is characteristic in Faradaic reactions in the anode for an LIB [9,21]. At the highest frequency, the intercept resistance in Z_{real} axis (R_b) corresponded to a bulk electrolyte resistance between working and counter electrode [21,22]. R_b of TSC-1 and -3 were identical, indicative of same cell structure. In this figure, the resistance from the highly distributed semi-circle (R_s) can include overall electrical/electrolyte conduction within the electrode or ionic transport within the surface film [9,21]. R_s of TSC-3 was larger than that of TSC-1, indicating a larger resistance and a low rate capability. Although a resistance corresponding to the charge transfer reaction at the interface was hard to locate, a sloped straight line with a decreasing frequency exhibited a different behavior in TSC-1 and -3 electrodes. The slope of TSC-1 electrode was steeper than that of TSC-3, indicative of more polarizable electrode feature caused by a smaller Faradaic peak in Fig. 8.

Fig. 10 displays the rate capability and cyclability of TSC electrodes. As for the rate capability, TSC-2 electrode showed a slightly higher rate performance as 53% at 150 mA g⁻¹ current rate. Because the alloying–dealloying process of SnO₂ is the most sluggish process, it is expected that a lower SnO₂ fraction should result in a better rate performance but the observed low rate capability in TSC-1 electrode is probably due to a retarded Li⁺ transport in less-developed mesostructure and a low Li⁺ solid-state diffusion within smaller TiO₂ crystals [21]. In Fig. 10(b), cycle performance was investigated for three electrodes until 40 cycles at 30 mA g⁻¹ current rate. For TSC-1 and -3 electrodes, a decrease of capacity was observed until five cycles and stable cycle performance appeared afterward. In TSC-2 electrode, an invariant capacity change

was observed, indicative of a good cyclability. The capacity retentions after 40 cycles were compared at Table 1. As seen, TSC-2 electrode showed a very good cycle performance (95.3% retention), while the cycle performances in TSC-1 and -3 electrodes were not satisfactory. In order to investigate a change of capacity contribution after cycles, the differential capacities per voltage of TSC-2 and -3 electrodes after 40 cycles were compared in Fig. 11. In TSC-2 electrode, shape and position of peaks remained invariant. On the contrary, a large peak change was observed in TSC-3 electrode, which displayed that the peak at 1.0 V was collapsed severely, while the decrease of peak intensity of the other two peaks was small. This indicated that the charging–discharging behavior of TSC-3 electrode after long cycles became similar to the conventional SnO₂ electrode [5,20]. As for TSC-2 electrode, the stable nanostructure maintained after long cycles, which was probably attributed to a high interaction between its components with an optimized TiO₂ crystal size.

4. Conclusions

Using the tetra-constituent co-assembly (Tetra-CCA) method based on the acid–base pair between Sn and Ti precursors, novel mesoporous carbon–TiO₂–SnO₂ nanocomposite materials were prepared. Here, the influence of SnO₂ amount was investigated. According to SnO₂ increase, the ordered mesoporous structure was initially observed but its collapse happened afterward. Furthermore, nanosized anatase TiO₂ crystals were embedded within the amorphous SnO₂ and carbon matrix and their size became larger. When applied into anode materials in lithium ion batteries, the discharge capacity and the initial efficiency became larger. For the electrode material containing large crystal TiO₂, it exhibited a reversible capacity of 378 mAh g⁻¹ and a very high utilization of TiO₂ for lithium storage (275 mAh g⁻¹). However, a high rate performance and a very stable cycle performance were observed in the nanocomposite electrode with 28.8% TiO₂, which was attributed to the stable nanostructure after long cycles.

Acknowledgement

This research was supported by a institutional support by KRICT and a grant from the fundamental R & D program for core technology of materials (TS117-17-1) funded by the Ministry of Knowledge Economy, Republic of Korea.

References

- [1] G.L. Xu, S.R. Chen, J.T. Li, F.S. Ke, L. Huang, S.G. Sun, J. Electroanal. Chem. 656 (2010) 185–191.
- [2] Y. Ishii, Y. Kanamori, T. Kawashita, I. Mukhopadhyay, S. Kawasaki, J. Phys. Chem. Solids 71 (2010) 511–514.
- [3] Y. Zhou, Y. Kim, C. Jo, J. Lee, C.W. Lee, S. Yoon, Chem. Commun. 47 (2011) 4944–4946.
- [4] H.J. Liu, S.H. Bo, W.J. Cui, F. Li, C.X. Wang, Y.Y. Xi, Electrochim. Acta 53 (2008) 6497–6503.
- [5] J. Fan, T. Wang, C.Z. Yu, B. Tu, Z.Y. Jiang, D.Y. Zhao, Adv. Mater. 16 (2004) 1432–1436.
- [6] Z. Bing, Y. Yuan, Y. Wang, Z.W. Fu, Electrochem. Solid-State Lett. 9 (2006) A101–A104.
- [7] Y.S. Hu, L. Kienle, Y.-G. Guo, J. Maier, Adv. Mater. 18 (2006) 1421–1426.
- [8] M.A. Reddy, M.S. Kishore, V. Pralong, V. Caignaert, U.V. Varadaraju, B. Raveau, Electrochem. Commun. 8 (2006) 1299–1303.
- [9] S. Yoon, B.H. Ka, C. Lee, M. Park, S.M. Oh, Electrochem. Solid-State Lett. 12 (2009) A28–A32.
- [10] L.J. Fu, H. Liu, H.P. Zhang, C. Li, T. Zhang, Y.P. Wu, H.Q. Wu, J. Power Sources 159 (2006) 219–222.
- [11] A.R. Armstrong, G. Armstrong, J. Canales, P.G. Bruce, Angew. Chem., Int. Ed. 43 (2004) 2286–2288.
- [12] A.R. Armstrong, G. Armstrong, J. Canales, P.G. Bruce, Adv. Mater. 17 (2005) 862–865.
- [13] M.A. Reddy, M.S. Kishore, V. Pralong, V. Caignaert, U.V. Varadaraju, B. Raveau, Electrochem. Solid-State Lett. 10 (2007) A29–A31.
- [14] A. Kuhn, R. Amandi, F.G. Alvarado, J. Power Sources 92 (2001) 221–227.

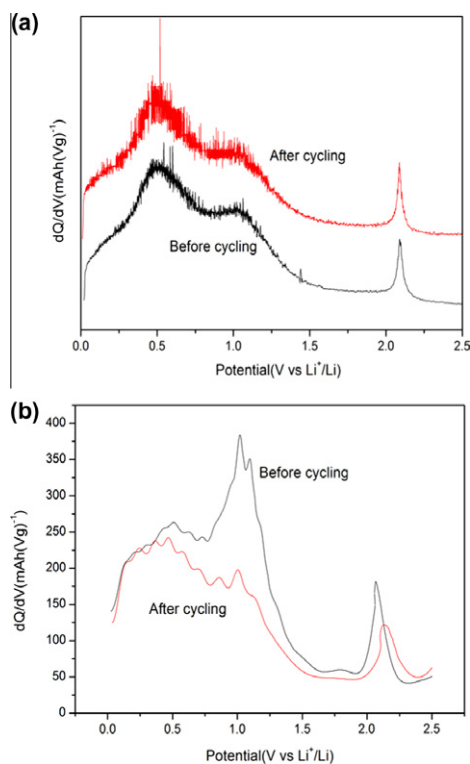


Fig. 11. Differential capacity per voltage vs. voltage profiles of TSC-2 electrode before cycling and after cycling (a). TSC-3 electrode before cycling and after cycling (b).

- [15] X. Qian, Y. Wan, Y. Wen, N. Jia, H. Li, D. Zhao, J. Colloid Interf. Sci. 328 (2008) 367–373.
- [16] D. Li, H. Zhou, I. Honma, Nat. Mater. 3 (2004) 65–72.
- [17] B. Tian, X. Liu, B. Tu, C. Yu, J. Fan, L. Wang, S. Xie, G.D. Stucky, D. Zhao, Nat. Mater. 2 (2003) 159–163.
- [18] B. Erdem, R.A. Hunsicker, G.W. Simmons, E.D. Sudol, V.L. Dimonie, M.S. El-Aasser, Langmuir 17 (2001) 2664–2669.
- [19] M. Oku, H. Matsuta, K. Wagatsuma, Y. Wasedab, S. Kohikic, J. Electron. Spectrosc. 105 (1999) 211–218.
- [20] M. Gao, X. Chen, H. Pan, L. Xiang, F. Wu, Y. Liu, Electrochim. Acta 55 (2010) 8067–8071.
- [21] S. Yoon, J. Lee, T. Hyeon, S.M. Oh, J. Electrochem. Soc. 147 (2000) 2507–2512.
- [22] J. Lee, S. Yoon, S.M. Oh, T. Hyeon, Adv. Mater. 12 (2000) 359–362.
- [23] J. Lee, S. Yoon, S.M. Oh, T. Hyeon, Chem. Commun. 21 (1999) 2177–2178.
- [24] J. Lee, M.C. Orilall, S.C. Warren, M. Kamperman, F.J. Disalvo, U. Wiesner, Nat. Mater. 7 (2008) 222–228.